Hydrodynamic Force Decoupling Using a Distributed Sensory System

Kevin Nelson and Kamran Mohseni, *Senior Member, IEEE*

***Abstract*—In this letter, we present a distributed pressure sensory system, inspired by the lateral line found in fish, for estimating hydrodynamic forces acting on an autonomous underwater vehicle. By canceling these forces using the vehicle control system, the dynamics of the vehicle can be decoupled from the state of the surrounding fluid. We discuss a control scheme which combines the measured hydrodynamic forces with a feedback controller that is robust to disturbances and measurement errors, achieving asymptotic tracking in the presence of bounded disturbances and errors. We compare this robust lateral line controller to a baseline robust controller not using the lateral line system and to a controller using the lateral line with simple PD feedback. We simulate a spatially and time varying velocity flow field on the scale of the vehicle and show that the robust lateral line controller has improved performance compared to both the baseline robust controller and the PD controller using the lateral line system.**

***Index Terms*—Marine robotics, sensor-based control, motion control.**

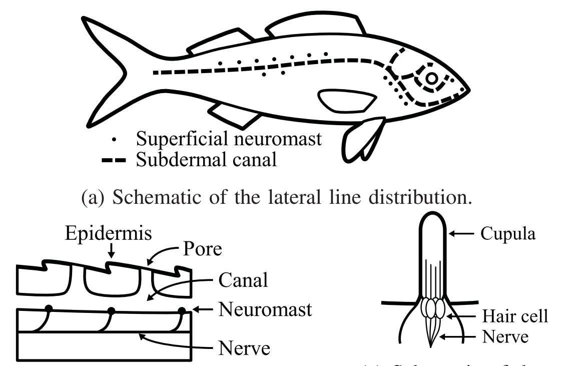

(a) Schematic of the lateral line distribution.

(b) Schematic of the canal neuromast

(c) Schematic of the superficial neuromast.

Fig. 1. Fish and other aquatic organisms have evolved a sensory system known as the lateral line to identify information about their fluid environment, from [14].

I. Introduction

MARINE vehicles operate in dynamic fluid environments, such as oceans and seas. While the dynamics of a marine vehicle can be represented by a finite number of ODEs, the fluid dynamics are governed by the Navier-Stokes equations, a set of partial differential equations. The environment has a strong coupling to the dynamics of the vehicle which manifests as pressure and shear stress distributions over the hull of the vehicle. These pressure and shear distributions result in hydrostatic and hydrodynamic forces, which can be decomposed into added mass forces, pressure and viscous damping, buoyant and restoring forces, and wave forces [1].

Historically, control engineers have dealt with this coupling by using Taylor series expansions to approximate the fluid interaction forces as functions of the vehicle state. This allows the kinetic equations to be written as functions of the vehicle velocity relative to the fluid, rather than as a function of the entire fluid state. However, this approximation can lead to inaccuracies when the background flow is dynamic and the scale is smaller than the vehicle length. There have been several control techniques employed to account for hydrodynamic forces, such as disturbance velocity estimators [2], sliding mode [3], [4] and adaptive [5]–[7] controllers, Kalman filter based velocity/disturbance estimators [8], [9], neural network or machine learning based estimators [10], [11], and robust nonlinear controllers [12]. These techniques have varying degrees of success, but all suffer from the same flaw: they attempt to determine an integral quantity, the total hydrodynamic force, from a single local measurement, the relative velocity of the vehicle with respect to the flow.

However, while control engineers have been attempting to design control techniques to achieve good performance, fish and other marine organisms have been performing maneuvers in the dynamic fluid environment they inhabit. Fish have evolved a sensory system, known as the lateral line [13], containing a distribution of specialized hair cell receptors called neuromasts to directly measure the pressure and velocity distributions over the surface of their body (see Fig. 1(a)). Most lateral lines systems contain two distinct types of neuromasts: sub-dermal canal neuromasts (shown in Fig. 1(b)) and superficial neuromasts (shown in Fig. 1(c)). Researchers suggest that the physiology of the neuromasts diverged to provide sensitivity to complimentary information about the surrounding fluid. For example, superficial neuromasts respond to lower frequency signals, whereas canal neuromasts respond to higher frequency signals [15]. Additionally, superficial neuromasts are believed to measure the

Manuscript received September 10, 2019; accepted February 9, 2020. Date of publication February 26, 2020; date of current version March 7, 2020. This letter was recommended for publication by Associate Editor M. Dunbabin and Editor J. Roberts upon evaluation of the reviewers' comments. This work was supported by the Office of Naval Research (ONR) and the National Science Foundation (NSF). *(Corresponding author: Kamran Mohseni.)*

Kevin Nelson is with the Department of Electrical and Computer Engineering, University of Florida, Gainesville, FL 32611 USA (e-mail: kjnelson@ufl.edu).

Kamran Mohseni is with the Department of Mechanical and Aerospace Engineering, Department of Electrical and Computer Engineering, and Institute for Networked Autonomous Systems, University of Florida, Gainesville, FL 32611 USA (e-mail: mohseni@ufl.edu).

Digital Object Identifier 10.1109/LRA.2020.2976331

relative flow velocity over the skin of the organism [16] whereas canal neuromasts measure the acceleration of the fluid [17]. Many researchers believe that fish use the lateral line in many behaviors such as rheotaxis [18], schooling [19], detection of obstacles and other organisms [20], predation [21], and communication [22].

Seeing the benefit that the lateral line provides to aquatic organisms has inspired many researchers to attempt to replicate the sensing capabilities of this system for use in robotic applications. Ren and Mohseni developed theoretical models showing the application of the lateral line to wake detection [23] and wall detection [24]. Some researchers have fabricated custom sensors to perform various task such as to measure flow rates [25]–[27] and detect dipoles [28], [29]. However, manufacturing custom sensors adds additional complexities, leading many researchers to use off-the-shelf sensors to replicate the functionality of the lateral line. Some researchers have used absolute pressure sensors, for example, in [30], a linear array of absolute pressure sensors was used in an attempt to determine the position, shape, and size of various objects in a flow. In another work [31], absolute pressure sensors were used to detect the angle of attack of a marine craft for use in active yaw control; the system was able to achieve reasonable results after advanced filtering techniques were applied. Chambers, *et al.*, attempted to use absolute pressure sensors to detect the turbulent wake of a cylinder [32]; these sensors suffered from low resolution, requiring amplification and high precision analog-to-digital converters to achieve moderate sensor resolution. Free and Paley showed that pressure sensors could be used to detect a Kármán vortex street behind an obstacle [33]. Other researchers have shown that a robotic fish with absolute pressure sensors can perform wall following [34]. In underwater applications, the signal measured by absolute pressure sensors is generally dominated by the large static pressure of the water column. This necessitates that the sensors have a large sensing range which leads to a reduction in the sensitivity of the sensor. Conversely, differential pressure sensors measure the pressure difference between two ports; the static pressure is thus a function of the vertical separation of the ports, which is generally much smaller than the height of the water column. Thus, differential pressure sensors can have a smaller sensing range leading to an increased sensitivity. For many applications where absolute pressure is not needed, the sensitivity of the sensor is more important than the range, leading to differential pressure sensors being desirable. Xu and Mohseni used differential pressure sensors to perform hydrodynamic force estimation [14] and wall-detection [35]. Differential pressure sensors have also been used to measure the relative velocity of a vehicle [36], achieving better accuracy at higher velocities; this setup was later validated in field tests [37].

In this letter, we use a distributed pressure sensory system to directly measure the hydrodynamic forces acting on an autonomous underwater vehicle (AUV) and decouple these forces from the rigid body dynamics. If the hydrodynamic forces can be measured and compensated for perfectly, the dynamics of the AUV effectively reduce to that of a rigid body in a vacuum. This approach is fundamentally different from traditional methods, which approximate the hydrodynamic forces as a function of a uniform flow over the vehicle; these traditional techniques break down when the flow is not approximately uniform at the vehicle scale. This continues our previous studies on the lateral line and its application to vehicle control. We first proposed the idea of using the lateral line system for AUV control in [14]. To validate the ability of the sensory system to measure hydrodynamic forces, we created a prototype vehicle mock-up with pressure sensors directly embedded into a PVC tube [35]. Rather than making costly modifications to the hull of our underwater vehicle, we developed a modular lateral line system composed of differential pressure sensors and presented the design and validation of the system in [38]. Additionally, in [39], we used our underwater vehicle to experimentally validate this scheme by performing station-keeping in the presence of arbitrary disturbances using the lateral line combined with a proportional derivative (PD) feedback controller. This letter differs from our previous work by presenting an improved sensor fusion algorithm, using a nonlinear controller that is robust to measurement and model errors rather than a simple PD controller, and by performing trajectory tracking, as opposed to station-keeping. Trajectory tracking adds additional complexity over station-keeping, since there are non-vanishing inertial and Coriolis forces due to vehicle velocities and accelerations. Typically, nonlinear controllers use robust and adaptive feedforward techniques to compensate for these forces. In this work, we use an adaptive term to compensate for inertial and Coriolis forces that arise due to the trajectory. We present simulation results to validate the fusion algorithm and control scheme by simulating the vehicle in a double-gyre inspired background flow and show that the lateral line with a robust nonlinear controller outperforms both the same controller without the lateral line system and a simple PD controller with the lateral line system.

The paper is organized as follows. In Section II, we present a model of the vehicle dynamics, the hydrodynamic force coupling, and a nonlinear controller. Section III presents an algorithm for calculating the hydrodynamic force from the discrete pressure measurements of a distributed pressure sensory system. Section IV presents a numerical simulation which we use to validate our control scheme by simulating an AUV with a lateral line in a spatially and time varying velocity field. In Section V, we discuss the results of the simulation and in Section VI we provide concluding remarks.

II. Background

A. Vehicle Model

One of the most general formulations of underwater vehicle dynamics is given by the governing equations for a rigid body with external forces [1]:

$$M_{\mathrm{RB}}\dot{\boldsymbol{\nu}} + C_{\mathrm{RB}}(\boldsymbol{\nu})\boldsymbol{\nu} = \boldsymbol{\tau}_{\mathrm{RB}}, \tag{1a}$$

$$\dot{\boldsymbol{\eta}} = J(\boldsymbol{\eta})\boldsymbol{\nu}, \tag{1b}$$

where the vector $\boldsymbol{\eta} \in \mathbb{R}^n$ contains the position and orientation of the vehicle in the inertial frame and $\boldsymbol{\nu} \in \mathbb{R}^n$ contains the linear and angular velocity of the vehicle expressed in the body-fixed frame with n representing the number of states. $M_{\mathrm{RB}} \in \mathbb{R}^{n\times n}$

is a matrix containing the inertial terms of the rigid body, $C_{\mathrm{RB}} : \mathbb{R}^n \to \mathbb{R}^{n\times n}$ is a matrix containing the Coriolis/centrifugal terms of the rigid body, which is a function of the which is a function of the body-frame velocities, $J : \mathbb{R}^n \to \mathbb{R}^{n\times n}$ represents the velocity transformation from the body-fixed frame to the inertial frame, and $\boldsymbol{\tau}_{\mathrm{RB}} \in \mathbb{R}^n$ is a vector of external forces and moments acting on the rigid body. The vector of external forces and moments can be written as

$$\boldsymbol{\tau}_{\mathrm{RB}} = \boldsymbol{\tau}_{\mathrm{grav}} + \boldsymbol{\tau}_{\mathrm{fluid}} + \boldsymbol{\tau}_{\mathrm{dist}} + \boldsymbol{\tau}_{\mathrm{c}}, \tag{2}$$

where $\boldsymbol{\tau}_{\mathrm{grav}}$ is a vector of gravitational forces and moments, $\boldsymbol{\tau}_{\mathrm{fluid}}$ is a vector of hydrodynamic and hydrostatic forces and moments, $\boldsymbol{\tau}_{\mathrm{dist}}$ is a vector of unmodeled disturbance forces and moments, and $\boldsymbol{\tau}_{\mathrm{c}}$ is a vector of control and propulsive forces and moments.

These external forces are functions of both the vehicle state and the external environment state, which is, in general, infinite dimension and governed by complex partial differential equations. For example, the hydrodynamic force/moment term, $\boldsymbol{\tau}_{\mathrm{fluid}}$, is dependent on both the state of the fluid and the state of the vehicle within the fluid, with the state of the fluid being continuous in both space and time and governed by the Navier-Stokes equation. However, it is difficult to fully observe the state of the environment, which leads us to seek a reduced order model that will provide sufficient accuracy for vehicle control. Historically, these forces have been approximated as functions of the vehicle states, i.e., these forces are linearized with respect to the vehicle velocities and accelerations. This leads to the dynamics of underwater vehicles generally being modeled by the following set of differential equations which are functions of the vehicle states [1]:

$$\begin{aligned} &M_{\mathrm{RB}}\dot{\boldsymbol{\nu}} + C_{\mathrm{RB}}(\boldsymbol{\nu})\boldsymbol{\nu} + M_{\mathrm{A}}\dot{\boldsymbol{\nu}} + C_{\mathrm{A}}(\boldsymbol{\nu})\boldsymbol{\nu} \\ &\quad + D(\boldsymbol{\nu})\boldsymbol{\nu} + g(\boldsymbol{\eta}) + \boldsymbol{\tau}_{\mathrm{dist}} = \boldsymbol{\tau}_c, && \text{(3a)} \\ &\dot{\boldsymbol{\eta}} = J(\boldsymbol{\eta})\boldsymbol{\nu}, && \text{(3b)} \end{aligned}$$

where $M_{\mathrm{A}} \in \mathbb{R}^{n\times n}$ represents the added mass matrix of the fluid, $C_{\mathrm{A}} : \mathbb{R}^n \to \mathbb{R}^{n\times n}$ is the Coriolis/centrifugal terms of the added mass, $D : \mathbb{R}^n \to \mathbb{R}^{n\times n}$ represents the drag terms, $g : \mathbb{R}^n \to \mathbb{R}^n$ represents the gravitational and buoyancy forces and moments, and $\boldsymbol{\tau}_{\mathrm{dist}} \in \mathbb{R}^n$ represents any unmodeled or disturbance forces and moments. However, the fluid forces and moments can be highly nonlinear and not well approximated by this model, leading to large disturbance forces and moments. In the next section, we will discuss how to directly calculate the fluid forces from the surface pressure and shear distribution, rather than approximating these forces as a function of the vehicle state.

B. Hydrodynamic Forces and Moments

The total force acting on the rigid body due to the fluid can be calculated from the surface integral of the pressure and shear stress distributions over the surface of the vehicle [40], i.e.,

$$\mathbf{f}_{\mathrm{fluid}} = -\int_S p\hat{\mathbf{n}}dS + \int_S \frac{1}{Re}\omega \times \hat{\mathbf{n}}dS, \tag{4}$$

where p is the pressure distribution over the vehicle's surface, S, $\hat{\mathbf{n}}$ is the normal vector, Re is the Reynolds number, and $\omega = \nabla \times u(\mathbf{x}, t)$ where u is the fluid velocity. The fluid moments on the vehicle can be found by,

$$\mathbf{m}_{\mathrm{fluid}} = -\int_S \mathbf{r} \times (p\hat{\mathbf{n}})dS + \int_S \frac{1}{Re}\mathbf{r} \times \omega \times \hat{\mathbf{n}}dS \tag{5}$$

where $\mathbf{r}$ is the moment arm. Aggregating the forces and moments into a single vector yields $\boldsymbol{\tau}_{\mathrm{fluid}} = [\mathbf{f}_{\mathrm{fluid}}^{\mathrm{T}}, \quad \mathbf{m}_{\mathrm{fluid}}^{\mathrm{T}}]^{\mathrm{T}}$.

Hence, for an incompressible fluid, the coupling of between the fluid environment and the vehicle dynamics is not a function of the entire fluid state, but rather a subset of the fluid state, i.e., the fluid state at the surface of the vehicle. If the pressure and shear distribution over the surface of the vehicle can be measured, then the fluid forces and moments can be calculated directly from eq. (4) and eq. (5), respectively. Furthermore, if these forces and moments are injected into a vehicle control system and adequate control authority is available, these forces and moments can be counteracted by the control system, effectively decoupling the vehicle dynamics from the fluid environment, reducing the dynamics to that of a rigid body in a vacuum.

Two simplifications can be made to the vehicle model and the fluid force estimator. First, many underwater vehicles are designed to be neutrally buoyant so that the weight is in equilibrium with the buoyant force. Thus, the gravitational force, $\boldsymbol{\tau}_{\mathrm{grav}}$, no longer needs to be tracked. However, the pressure distribution includes the hydrostatic pressure, in addition to the dynamic pressure, which, when integrated, produces the buoyant force acting on the vehicle. Since the buoyant force is already being compensated by the weight of the vehicle, if the total pressure distribution is integrated and the resultant force is fed into the controller without first compensating for the hydrostatic pressure, the inverse of the buoyant force will be erroneously added into the control signal. To compensate, the hydrostatic pressure is removed from the pressure distribution before the surface integration is performed. A method for removing the hydrostatic pressure is described in [39].

Second, a simplification can be made to the fluid force calculation by noticing that the component of the force due to the pressure dominates the component due to the shear stress for high Reynolds number objects. The Reynolds number is a nondimensional number given by the equation $Re = \rho UL/\mu$, where ρ is the density of the fluid, U is the velocity of the fluid, L is the characteristic length dimension, and μ is the dynamic viscosity of the fluid. Due to the high density of water, AUVs typically operate at Reynolds numbers of greater than 10^4. Thus, the fluid forces acting on the rigid body are dominated by the pressure forces and the hydrodynamic force can be approximated as the surface integral of the pressure distribution.

C. Control Scheme

If the above approximations hold, the fluid states can be decoupled from the vehicle states by directly measuring and integrating the hydrodynamic pressure distribution and feeding the resultant hydrodynamic force into the motion controller. The

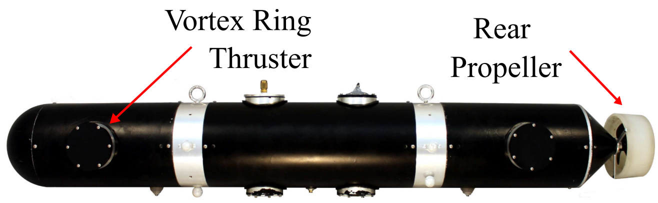

Fig. 2. Picture of CephaloBot, our in-house developed AUV.

dynamics can be rewritten as

$$M_{\text{RB}}\dot{\boldsymbol{\nu}} + C_{\text{RB}}(\boldsymbol{\nu})\boldsymbol{\nu} + \boldsymbol{\tau}_{\text{hyd}} + \boldsymbol{\tau}_{\text{dist}} = \boldsymbol{\tau}_{\text{c}}, \tag{6a}$$

$$\dot{\boldsymbol{\eta}} = J(\boldsymbol{\eta})\boldsymbol{\nu}, \tag{6b}$$

where $\boldsymbol{\tau}_{\text{hyd}}$ is a vector of hydrodynamic forces and moments resulting from the pressure distribution on the surface the rigid body and $\boldsymbol{\tau}_{\text{dist}}$ are the unmodeled disturbance forces (which includes the residual unmeasured forces due to the shear stress). The vector of control forces and moments can be written as

$$\boldsymbol{\tau}_{\text{c}} = \hat{\boldsymbol{\tau}}_{\text{hyd}} + \boldsymbol{\tau}_{\text{FB}}, \tag{7}$$

where $\hat{\boldsymbol{\tau}}_{\text{hyd}}$ is the measured hydrodynamic forces and $\boldsymbol{\tau}_{\text{FB}}$ is a stabilizing feedback term. Using Lyapunov analysis, a nonlinear controller can be designed that is robust to disturbances and measurement errors [41]. This controller applies to affine in the control systems, which includes the dynamics in eq. (6). For these dynamics, a stabilizing control law can be defined as

$$\boldsymbol{\tau}_{\text{FB}} = Y\hat{\theta} + J(\eta)^{\text{T}} \left[K_s \mathbf{s} + \int_0^t (K_s \mathbf{s} + \beta \text{sgn}(\mathbf{s}))\, dt \right], \tag{8}$$

with adaptive update law

$$\dot{\hat{\theta}} = \Gamma Y^{\text{T}} J^{\text{T}} \mathbf{s}, \tag{9}$$

where $\mathbf{s} = \dot{\tilde{\eta}} + \alpha\tilde{\eta}$ is the filtered error system, Y is the regression matrix of known dynamics, $\hat{\theta}$ is an estimate of the unknown model parameters, and K_s, α, β, and Γ are controller gains. The adaptive terms, $Y\theta$, are designed to learn the inertial and Coriolis parameters of the rigid body. This controller is capable of achieving asymptotic tracking which can be proved with Lyapunov stability analysis. A similar controller without a hydrodynamic force compensator was derived with stability analysis in [12]; for brevity, the stability analysis is not shown here.

III. Methodology

To validate the robust controller and hydrodynamic force compensation, we developed a measurement algorithm to calculate the forces from a distributed pressure system. This system was designed for use with our in-house-developed underwater vehicle, CephaloBot, shown in Fig. 2. Extensive details describing CephaloBot's design and systems can be found in [42].

In this study, we will approximate CephaloBot's geometry as a cylinder and derive the sway, heave, yaw, and pitch components of the hydrodynamic force. Thus, the hydrodynamic force is the surface integral of the pressure distribution over a cylinder, that

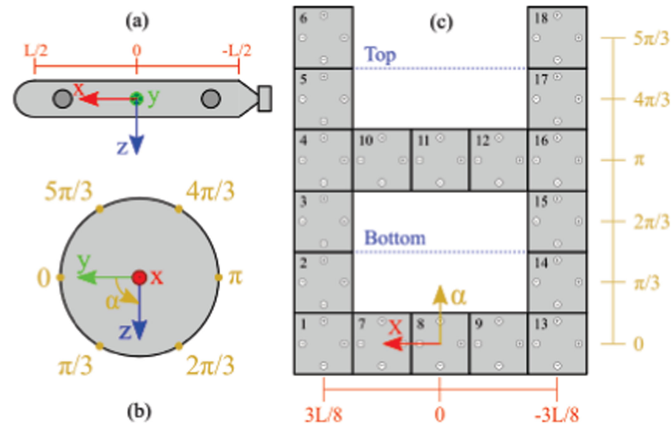

Fig. 3. Diagram of the distribution of sensor modules over CephaloBot. (a) Shows the body frame coordinate system which is affixed to the center of volume of CephaloBot. (b) Shows a cross-section of CephaloBot with module axial locations marked in yellow. (c) Shows the sensor module distribution: the modules are organized into two rings of six modules with an additional six modules connecting the two rings (for a total of eighteen modules).

is,

$$\mathbf{f}_{\text{hyd}} = R \int_{-L/2}^{L/2} \int_0^{2\pi} p\,(\alpha, x)\, \hat{\mathbf{n}} d\alpha dx \tag{10}$$

where α represents the azimuthal angle and the unit normal vector is $\hat{\mathbf{n}} = [0 \quad \cos\alpha \quad \sin\alpha]^{\text{T}}$. Performing the azimuthal integration gives the force per unit length, that is,

$$\frac{d\mathbf{f}_{\text{hyd}}(x)}{dx} = R \oint_0^{2\pi} p\,(\alpha, x)\, \hat{\mathbf{n}} d\alpha. \tag{11}$$

Assuming that the azimuthal pressure distribution at a given axial location x can be represented by a Fourier series, then the orthogonality of trigonometric functions can be used to show that that the hydrodynamic force due to the pressure distribution is only dependent on the first Fourier sine and cosine coefficients of the azimuthal pressure distribution. That is, the sway component of the force acting on the body section depends on the first cosine coefficient of the azimuthal pressure distribution and the heave component depends on the first sine coefficient. Additionally, the yaw and pitch moments can be calculated from the sway and heave force per length distribution as in eq. (5). A vectorial equation for the hydrodynamic force can be written as

$$\boldsymbol{\tau}_{\text{hyd}} = \pi R \int_{-L/2}^{L/2} \Pi(x) dx, \tag{12}$$

where $\Pi(x) = [0 \quad a_1(x) \quad b_1(x) \quad 0 \quad xb_1(x) \quad xa_1(x)]^{\text{T}}$.

Equation (12) suggests that instead of needing to measure the full azimuthal pressure distribution over the body, due to orthogonality, it is only necessary to measure sufficient information to calculate the first Fourier mode of the pressure distribution. To this end, we organized the lateral line into two rings of six evenly spaced sensors as shown in Fig. 3. From the discrete pressure measurements, the first Fourier coefficients can be calculated at the two rings. We discuss a method for fitting these modes to discrete measurements made by differential pressure sensors in [39]. Since we want the coefficients as a function of distance along the length of the vehicle, we placed additional pressure sensors in between the two rings which are used to interpolate the coefficient between the rings. In [39], we assumed a linear flow distribution between the two rings and linearly interpolated $a_1(x)$ between the rings. In this work, instead of assuming a linear flow distribution, we fit a function to the pressure measurements of the intermediate sensors and interpolate $a_1(x)$ using this function.

IV. Simulation Results

A. Simulation Setup

To validate the proposed sensory system and control scheme, we developed a numerical simulation to simulate the model of an underwater vehicle's dynamics given in eq. (6) and the effects of a spatially and time varying background flow on the vehicle. The simulation uses a fourth-order Runge-Kutta solver to integrate the rigid body dynamics and external forces.

1) Vehicle Model: For this simulation, we modeled our custom AUV, CephaloBot. For actuation, the vehicle is equipped with a rear propeller and four vortex ring thrusters (VRTs). The rear propeller provides surge forces while the VRTs provide sway forces and yaw moments. For this simulation, we assume each thruster can provide a maximum force of 10 N and we assume that the thrusters do not impact the fluid or sensors. In a previous study [43], we experimentally determined the model coefficients for CephaloBot which we use here. The vehicle model matrices are

$$M = \mathrm{diag}(m + X_{\dot{u}},\ m + Y_{\dot{v}},\ I_z + N_{\dot{r}}),$$

$$C(\boldsymbol{\nu}) = \begin{bmatrix} 0 & 0 & -mv - Y_{\dot{v}} v_{\mathrm{rel}} \\ 0 & 0 & mu + X_{\dot{u}} u_{\mathrm{rel}} \\ mv + Y_{\dot{v}} v_{\mathrm{rel}} & -mu - X_{\dot{u}} u_{\mathrm{rel}} & 0 \end{bmatrix},$$

where m is the mass of the vehicle, I_z is the moment of inertia about the body z axis, $X_{\dot{u}}$ is the added mass along the body x axis due to a surge acceleration, $Y_{\dot{v}}$ is the added mass along the body y axis due to a sway acceleration, and $N_{\dot{r}}$ is the added moment of inertial about the body z axis due to a yaw rotation. The coefficients used are m=16.0 kg, I_z=2.27 kg m^2, $X_{\dot{u}}$=0.52 kg, $Y_{\dot{v}}$=1.97 kg, $N_{\dot{r}}$=0.0021 kg m^2.

2) Hydrodynamic Model: For this simulation, we use a hydrodynamic model derived from potential flow to generate the pressure distribution and hydrodynamic forces acting on the vehicle. To calculate the sway drag on the vehicle due to a uniform flow, we use the drag equation [44]

$$F_y = \frac{1}{2}\rho v_{\mathrm{rel}}^2 C_D(Re) A, \tag{13}$$

where ρ is the density of the fluid, v_{rel} is the relative flow velocity over the vehicle, C_D is the drag coefficient of the object which is a function of the Reynolds number, and A is the projected area. Since the Reynolds number is a function of the relative velocity, the drag force is a nonlinear function of the relative velocity which is not well approximated by a polynomial.

For a nonuniform flow, we modified eq. (13) to be

$$F_y = \frac{1}{2}\rho R \int_{-L/2}^{L/2} C_D(Re) v_{\mathrm{rel}}^2(x) dx, \tag{14}$$

where v_{rel} is a function of the distance, x, from the center of the vehicle. The relative velocity at a distance x is given by $v_{\mathrm{rel}}(x) = v + rx + v_{\mathrm{bg}}(x)$, where v is the velocity of the vehicle, r is the angular velocity of the vehicle, and v_{bg} is the sway component of the background flow velocity at position x. The yaw drag moment, M_ψ, can be calculate by multiplying the quantity inside the integral in eq. (14) by the distance along the body, x, before performing the integration.

To generate the pressure distribution acting on the surface of the vehicle, we used a modified potential flow model. In potential flow, the pressure distribution over an infinitely long cylinder in a flow is given by the equation [44]

$$p(\alpha) = p_\infty + \rho v_{\mathrm{rel}}^2 \left[\cos(2\alpha) - \frac{1}{2}\right] \tag{15}$$

where p_∞ is the free stream pressure, ρ is the density of the fluid, and v_{rel} is the relative velocity of the fluid. The potential flow model predicts zero drag force; therefore, we modify this model by adding a $\cos(\alpha)$ term so that after integrating the pressure distribution, the resulting force will be consistent with eq. (13). The modified pressure model is

$$p(\alpha) = p_\infty + \frac{\rho}{\pi} C_d(Re) v_{\mathrm{rel}}^2 \left[\cos(2\alpha) + \cos\alpha - \frac{1}{2}\right]. \tag{16}$$

To calculate the force due to added mass, we use the model from eq. (3). For the added mass coefficients, we use the fitted parameters from our study [43]. We then modify eq. (16) to account for the added mass, that is,

$$p(\alpha) = p_\infty + \frac{1}{2}\rho D \frac{m_a}{m} \frac{dv_{\mathrm{rel}}}{dt} \cos(\alpha) + \frac{\rho}{\pi} C_d(Re) v_{\mathrm{rel}}^2 \left[\cos(2\alpha) + \cos\alpha - \frac{1}{2}\right], \tag{17}$$

where m_a is the added mass coefficient, m is the mass of the vehicle, and D is the cross-sectional diameter of the vehicle. These modifications are made to simplify the complexity of the simulation and are not required for the proposed sensing algorithm, which remains valid for real world flow conditions as we have demonstrated our previous study [39].

3) Background Flow: To demonstrate the performance of the proposed controller in dynamic flow conditions, we used a model of a time-dependent double-gyre [45] to generate a temporally and spatially varying flow field. This model provides a simple analytical equation for a time dependent flow-field, not an approximate solution to the Navier-Stokes equations. This background flow is given by the stream-function

$$\phi(x, y, t) = A \sin(\pi f(x, y)) \sin(\pi y), \tag{18}$$

where $f(x,t) = a(t)x^2 + b(t)x$, $a(t) = \epsilon \sin(\omega t)$, and $b(t) = 1 - 2\epsilon \sin(\omega t)$. The parameter A affects the amplitude of the velocity field, ω is the period of oscillation, and ϵ affects the magnitude of oscillation in the x direction. The flow parameters used in

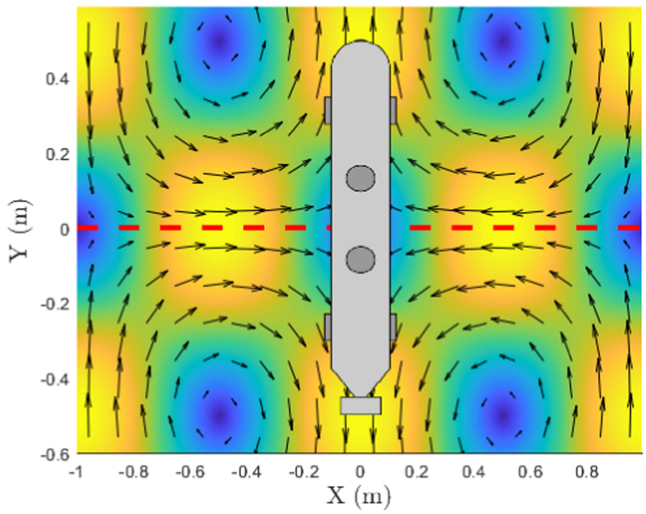

Fig. 4. Velocity field of the background flow, generated from eq. (18) at $t = 0$. The desired trajectory of the vehicle is shown by the red, dashed line.

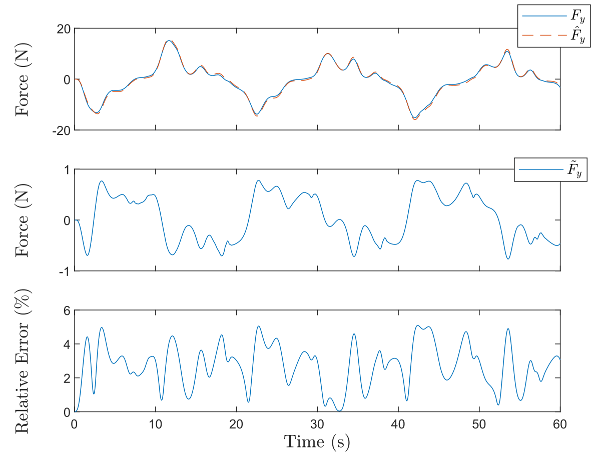

Fig. 5. Hydrodynamic sway forces from simulation of vehicle in test background flow. (Top) Hydrodynamic forces acting on the vehicle, F_y (shown by a solid blue line), compared to the forces measured by the lateral line, $\hat{F}_y$ (shown by a dashed red line). (Middle) Shows the measurement error, $\tilde{F}_y = F_y - \hat{F}_y$. (Bottom) Relative measurement error of the lateral line.

this simulation were $A = 0.1$ m/s, $\epsilon = 0.3$ m, and $\omega = 1$ rad. The velocity field can by calculated from the stream function given in eq. (18) by $\boldsymbol{\nu}_{\mathrm{bg}}(x, y, t) = [u_{\mathrm{bg}} \quad v_{\mathrm{bg}} \quad r_{\mathrm{bg}}]^{\mathrm{T}} = [-\frac{\partial \phi}{\partial y} \quad \frac{\partial \phi}{\partial x} \quad 0]^{\mathrm{T}}$. The resulting velocity field generated from eq. (18) at $t = 0$ is shown in Fig. 4.

B. Results

This section presents the results of the numerical simulation, described above. To validate the proposed hydrodynamic force compensation algorithm and control scheme, we simulated our AUV traveling through the dynamic background flow described above, using the lateral line system to measure the hydrodynamic forces and moments acting on the vehicle and directly compensating for them as described in Section II. For this simulation, the controller gains used are $K_s = 25, \alpha = 1, \beta = 1$, and $\Gamma = 1$. The desired trajectory was $\eta_d = [\sin(\frac{\pi}{10}t) \quad 0 \quad \frac{\pi}{2}]^{\mathrm{T}}$, which is shown as a dashed line in Fig. 4. This trajectory was chosen to maximize the sway hydrodynamic forces acting on the vehicle. The hydrodynamic forces acting on the vehicle during this simulation are shown in Fig. 5, along with the lateral line measurements and measurement errors; the maximum measurement error of the lateral line was 0.78 N, a relative error of 5.2%. The vehicle position, sway velocity, and controller force calculations during this simulation are shown in Fig. 6(a); this controller achieved a mean position error of 0.3 cm and an root-mean-square (RMS) position error of 1.3 cm.

For comparison, we also simulated a baseline robust nonlinear controller without a hydrodynamic force compensation system. This controller has the same form as the aforementioned controller, except that since the controller is not directly measuring the hydrodynamic forces, it assumes that the fluid interaction with the vehicle can be approximated as a function of the vehicle state as in eq. (3). The adaptive terms are designed accordingly, i.e., to adapt for added mass and linear and quadratic damping parameters in addition to the inertial and Coriolis parameters. The flow conditions, simulation parameters, and controller gains are identical to the previous controller. The results of this baseline controller are shown in Fig. 6(b), which achieved a mean position error of 4.4 cm and a RMS position error of 5.1 cm.

As a final comparison, we simulated the controller described in [39], which uses the hydrodynamic force compensation scheme described in this letter with a simple PD feedback structure. The simulation and flow parameters are identical to those listed above, with the controller gains identical to those reported in [39]. The performance of this controller is shown in Fig. 6(c); it achieves a mean position error of 24.3 cm and a RMS position error of 28.1 cm.

V. Discussion

These results show that the PD controller with hydrodynamic force compensation achieves worse performance than both robust nonlinear controllers. Theoretically, this controller is only able to achieve bounded tracking stability, rather than asymptotic tracking convergence, since it does not compensate for measurement errors or for the inertial and Coriolis forces due to the trajectory. However, this controller can achieve asymptotic regulation to a setpoint if it is assumed that the measurement error scales with velocity, since the inertial and Coriolis forces and the measurement error vanish as the vehicle converges to the desired setpoint.

While in theory both robust controllers confer asymptotic stability, these simulations show that the controller using the lateral line system to measure the hydrodynamic forces outperforms the baseline controller by a significant margin. This is due to the dynamic background flow, which varies both in space and in time, having a scale which is smaller than the vehicle scale. The baseline controller attempts to adapt for the fluid forces as a function of a single variable, the relative vehicle velocity, which is not valid at this spatial scale. Additionally, the integral term, which provides robustness to modeling errors, is not able to learn the disturbances quickly enough at the given

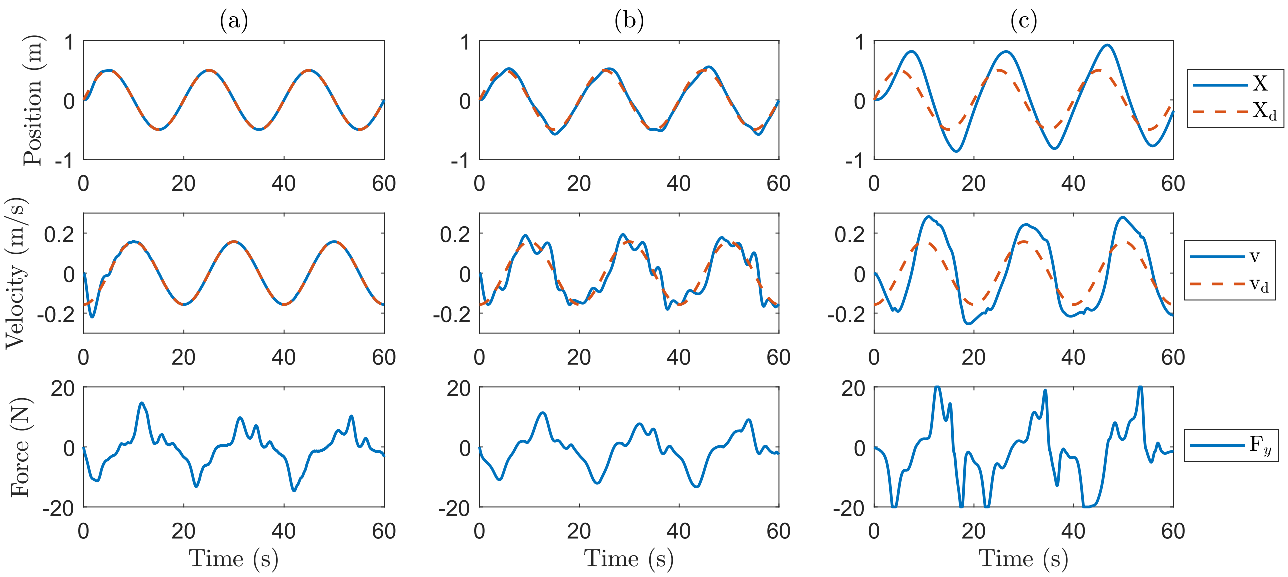

Fig. 6. Simulated results of the (a) robust nonlinear controller with hydrodynamic force compensation, (b) baseline robust controller, (c) PD controller with hydrodynamic force compensation. Actual trajectories are denoted by a solid blue line and desired trajectories are denoted by a dashed red line. (Top) The actual and desired inertial frame X trajectory. (Middle) The actual and desired sway velocities. (Bottom) The force commanded by the controller.

time scales. However, the lateral line is able to directly measure the hydrodynamic forces acting on the vehicle, which eliminates the majority of the complexity from the adaptive terms and any disturbance terms that must be compensated for by the integral term are small in comparison to the disturbances of the baseline controller.

In simpler flow conditions, for example with no background flow, the baseline controller can achieve comparable performance to the hydrodynamic force compensation controller. For missions in passive environments, it might make sense to forgo the additional costs of a distributed sensory system. However, as shown in this study, in dynamic flows, the lateral line can improve the overall performance of the system and thus is a desirable addition to an underwater vehicle. Additionally, though not presented in this study, a lateral line can be used to facilitate higher level decision making such as obstacle avoidance or background flow estimation. In future studies, we plan to investigate using the lateral line to facilitate these behaviors on an AUV in addition to using it for hydrodynamic force compensation. Additionally, we plan to extend the sensing capabilities to measure the surge forces acting on the vehicle.

VI. Conclusion

We presented a distributed sensory system capable of measuring the pressure distribution on a submerged autonomous underwater vehicle along with algorithms for calculating the hydrodynamic forces and moments from this distribution. Additionally, we presented a robust nonlinear controller that leverages these measurements to effectively decoupling the vehicle states from the fluid states. We developed a numerical simulation to validate our control algorithms and sensory system, and show that a controller which leverages this sensory system can outperform a modern robust nonlinear controller in a dynamic background flow.

References

[1] T. I. Fossen, *Handbook of Marine Craft Hydrodynamics and Motion Control*. Chichester, UK: John Wiley and Sons, 2011.

[2] G. Antonelli, F. Caccavale, S. Chiaverini, and L. Villani, “Tracking control for underwater vehicle-manipulator systems with velocity estimation,” *IEEE J. Ocean. Eng.*, vol. 25, no. 3, pp. 399–413, Jul. 2000. [Online]. Available: http://dx.doi.org/10.1109/48.855403

[3] D. Yoerger and J. Slotine, “Robust trajectory control of underwater vehicles,” *IEEE J. Ocean. Eng.*, vol. 10, no. 4, pp. 462–470, Oct. 1985.

[4] A. J. Healey and D. Lienard, “Multivariable sliding mode control for autonomous diving and steering of unmanned underwater vehicles,” *IEEE Journal Ocean. Eng.*, vol. 18, no. 3, pp. 327–339, Jul. 1993.

[5] G. Antonelli, S. Chiaverini, N. Sarkar, and M. West, “Adaptive control of an autonomous underwater vehicle: Experimental results on ODIN,” *IEEE Trans. Control Syst. Technol.*, vol. 9, no. 5, pp. 756–765, Sep. 2001.

[6] T. I. Fossen and S. I. Sagatun, “Adaptive control of nonlinear systems: A case study of underwater robotic systems,” *J. Field Robot.*, vol. 8, no. 3, pp. 393–412, 1991.

[7] J. Yuh, “Modeling and control of underwater robotic vehicles,” *IEEE Trans. Syst., Man Cybern.*, vol. 20, no. 6, pp. 1475–1483, Nov./Dec. 1990.

[8] D. B. Marco and A. J. Healey, “Local area navigation using sonar feature extraction and model-based predictive control,” *Int. J. Syst. Sci.*, vol. 29, no. 10, pp. 1123–1133, 1998.

[9] B. Allotta *et al.*, “A new AUV navigation system exploiting unscented kalman filter,” *Ocean Eng.*, vol. 113, pp. 121–132, 2016.

[10] T. W. Kim and J. Yuh, “A novel neuro-fuzzy controller for autonomous underwater vehicles,” in *Proc. IEEE Int. Conf. Robot. Autom.*, Seoul, Korea, May 2001, pp. 2350–2355.

[11] P. Walters, R. Kamalapurkar, F. Voight, E. M. Schwartz, and W. E. Dixon, “Online approximate optimal station keeping of a marine craft in the presence of an irrotational current,” *IEEE Trans. Rob.*, vol. 34, no. 2, pp. 486–496, Apr. 2018.

[12] N. Fischer, D. Hughes, P. Walters, E. Schwartz, and W. Dixon, “Nonlinear rise-based control of an autonomous underwater vehicle,” *IEEE Trans. Robot.*, vol. 30, no. 4, pp. 845–852, Aug. 2014.

[13] J. H. S. Blaxter, “Structure and development of the lateral line,” *Biol. Rev.*, vol. 62, no. 4, pp. 471–514, 1987.

[14] Y. Xu and K. Mohseni, “Bioinspired hydrodynamic force feedforward for autonomous underwater vehicle control,” *IEEE/ASME Trans. Mechatronics*, vol. 19, no. 4, pp. 1127–1137, Aug. 2014.

[15] A. B. A. Kroese and N. A. M. Schellart, "Velocity- and acceleration-sensitive units in the trunk lateral line of the canal," *J. Neurophysiology*, vol. 68, no. 6, pp. 2212–2221, 1992.

[16] A. B. A. Kroese, J. M. Van der Zalm, and J. Van den Bercken, "Frequency response of the lateral-line organ of *Xenopus laevis*," *Pflügers Archiv*, vol. 375, no. 2, pp. 167–175, 1978. [Online]. Available: http://dx.doi.org/10.1007/BF00584240

[17] H. Munz, "Functional organization of the lateral line periphery," in *The Mechanosensory Lateral Line*. Berlin, Germany: Springer, 1989, pp. 285–297.

[18] J. C. Montgomery, C. F. Baker, and A. G. Carton, "The lateral line can mediate rheotaxis in fish," *Nature*, vol. 389, no. 6654, pp. 960–963, 1997.

[19] T. J. Pitcher, B. L. Partridge, and C. S. Wardle, "A blind fish can school," *Science*, vol. 194, no. 4268, pp. 963–965, 1976.

[20] H. Bleckmann, "Peripheral and central processing of lateral line information," *J. Comp. Physiol. A Neuroethol. Sens. Neural Behav. Physiol.*, vol. 194, no. 2, pp. 145–158, 2008.

[21] S. Coombs, C. B. Braun, and B. Donovan, "The orienting response of Lake Michigan mottled sculpin is mediated by canal neuromasts," *J. Exp. Biol.*, vol. 204, pp. 337–348, 2001.

[22] M. Satou *et al.*, "Behavioral and electrophysiological evidences that the lateral line is involved in the inter-sexual vibrational communication of the himé salmon (landlocked red salmon, *Oncorhynchus nerka*)," *J. Comp. Physiol. A Neuroethol. Sens. Neural Behav. Physiol.*, vol. 174, no. 5, pp. 539–549, 1994.

[23] Z. Ren and K. Mohseni, "A model of the lateral line of fish for vortex sensing," *Bioinspiration Biomimetics*, vol. 7, no. 3, 2012, Art. no. 036016.

[24] Z. Ren and K. Mohseni, "Wall detection by lateral line sensory system of fish," in *Proceedings of the AIAA Aerospace Sciences Meeting*, MD, USA: National Harbor, Jan. 2014. [Online]. Available: http://dx.doi.org/10.2514/6.2014-0072

[25] Z. Fan, J. Chen, J. Zou, D. Bullen, C. Liu, and F. Delcomyn, "Design and fabrication of artificial lateral line flow sensors," *J. Micromech. Microeng.*, vol. 12, no. 5, pp. 655–661, 2002.

[26] A. Klein and H. Bleckmann, "Determination of object position, vortex shedding frequency and flow velocity using artificial lateral line canals," *Beilstein J. Nanotechnol.*, vol. 2, pp. 276–283, 2011.

[27] A. G. P. Kottapalli, C. W. Tan, M. Olfatnia, J. M. Miao, G. Barbastathis, and M. S. Triantafyllou, "A liquid crystal polymer membrane MEMS sensor for flow rate and flow direction sensing applications," *J. Micromech. Microeng.*, vol. 21, no. 8, pp. 1–11, 2011.

[28] A. Dagamseh, R. Wiegerink, T. Lammerink, and G. Krijnen, "Imaging dipole flow sources using an artificial lateral-line system made of biomimetic hair flow sensors," *J. R. Soc. Interface*, vol. 10, no. 83, 2013.

[29] A. T. Abdulsadda and X. Tan, "Underwater tracking of a moving dipole source using an artificial lateral line: Algorithm and experimental validation with ionic polymer–metal composite flow sensors," *Smart Mater. Struct.*, vol. 22, no. 4, 2013, Art. no. 045010.

[30] V. I. Fernandez, A. Maertens, F. M. Yaul, J. Dahl, J. H. Lang, and M. S. Triantafyllou, "Lateral-line-inspired sensor arrays for navigation and object identification," *Marine Technol. Soc. J.*, vol. 45, no. 4, pp. 130–146, 2011.

[31] A. Gao and M. Triantafyllou, "Bio-inspired pressure sensing for active yaw control of underwater vehicles," in *Proc. IEEE OCEANS Conf.*, Oct. 2012, pp. 14–19.

[32] L. Chambers *et al.*, "A fish perspective: detecting flow features while moving using an artificial lateral line in steady and unsteady flow," *J. The Roy. Soc. Interface*, vol. 11, no. 99, 2014, Art. no. 20140467.

[33] D. A. Paley and B. A. Free, "Model-based observer and feedback control design for a rigid Joukowski foil in a Karman vortex street," *Bioinsp. Biomim.*, vol. 13, 2018, Art. no. 035001.

[34] W. Yen, D. M. Sierra, and J. Guo, "Controlling a robotic fish to swim along a wall using hydrodynamic pressure feedback," *IEEE J. Ocean. Eng.*, vol. 43, no. 2, pp. 369–380, 2018.

[35] Y. Xu and K. Mohseni, "A pressure sensory system inspired by the fish lateral line: Hydrodynamic force estimation and wall detection," *IEEE J. Ocean. Eng.*, vol. 42, no. 3, pp. 532–543, Jul. 2017. [Online]. Available: http://dx.doi.org/10.1109/JOE.2016.2613440

[36] J. F. Fuentes-Pérez, C. Meurer, J. A. Tuhtan, and M. Kruusmaa, "Differential pressure sensors for underwater speedometry in variable velocity and acceleration conditions," *IEEE J. Ocean. Eng.*, vol. 43, no. 2, pp. 418–426, Apr. 2018.

[37] C. Meurer, J. Fuentes-Pérez, N. Palomeras, M. Carreras, and M. Kruusmaa, "Differential pressure sensor speedometer for autonomous underwater vehicle velocity estimation," *IEEE J. Ocean. Eng.*, 2019. [Online]. Available: https://doi.org/10.1109/JOE.2019.2907822

[38] K. Nelson and K. Mohseni, "Design of a 3-d printed, modular lateral line sensory system for hydrodynamic force estimation," *Marine Technol. Soc. J.*, vol. 51, no. 5, pp. 103–115, 2017.

[39] M. Krieg, K. Nelson, and K. Mohseni, "Distributed sensing for fluid disturbance compensation and motion control of intelligent robots," *Nature Mach. Intell.*, vol. 1, no. 5, pp. 216–224, 2019.

[40] G. K. Batchelor, *An Introduction to Fluid Dynamics*. Cambridge, UK: Cambridge University Press, 1967.

[41] B. Xian, D. M. Dawson, M. S. de Queiroz, and J. Chen, "A continuous asymptotic tracking control strategy for uncertain nonlinear systems," *IEEE Trans. Autom. Control*, vol. 49, pp. 1206–1211, Jul. 2004. [Online]. Available: http://dx.doi.org/10.1109/TAC.2004.831148

[42] M. Krieg, P. Klein, R. Hodgkinson, and K. Mohseni, "A hybrid class underwater vehicle: Bioinspired propulsion, embedded system, and acoustic communication and localization system," *Marine Technol. Soc. J.: Special Edition Biomimetics Marine Technol.*, vol. 45, no. 4, pp. 153–164, 2011.

[43] M. Krieg and K. Mohseni, "Comparison of different methods for estimating energetics related to efficiency on a UUV with cephalopod inspired propulsion," in *Proc. Int. Symp. Marine Propulsors*, Jun. 2017, pp. 12–15.

[44] L. M. Milne-Thomson, *Theoretical Aerodynamics*. Mineola, NY, USA: Dover, 1958.

[45] S. C. Shadden, F. Lekien, and J. E. Marsden, "Definition and properties of Lagrangian coherent structures from finite time Lyapunov exponents," *Physica D*, vol. 212, no. 3-4, pp. 271–304, 2005.